Chemical Science

ROYAL SOCIETY OF CHEMISTRY

EDGE ARTICLE

View Article Online
View Journal

Open Access Article. Published on 26 February 2026. Downloaded on 3/19/2026 5:43:23 PM.
This article is licensed under a Creative Commons Attribution-NonCommercial 3.0 Unported Licence.

Check for updates

Cite this: DOI: 10.1039/d5sc10183b

All publication charges for this article have been paid for by the Royal Society of Chemistry

Received 29th December 2025
Accepted 25th February 2026

DOI: 10.1039/d5sc10183b

rsc.li/chemical-science

Influence of aliovalent substitution on structure and dynamics in sodium halide $Na_{3-2x}Y_{1-x}Nb_xCl_6$ solid electrolytes

Brian B. Phan,[a] Tso Shuen,[b] Dmitry Vrublevskiy,[a] Qingyu Yan[b] and Vladimir K. Michaelis *[a]

Sodium halide solid electrolytes are garnering increased interest because of their synthetic flexibility to incorporate a variety of cations, thereby altering their structure and properties. Aliovalent substitution is said to increase ionic conductivity by promoting polyanion rotation. Herein, we synthesise and assess a series of $Na_{3-2x}Y_{1-x}Nb_xCl_6$, probing their complex structures using complementary powder X-ray diffraction and variable-temperature 1D and 2D solid-state nuclear magnetic resonance spectroscopy. The bond-valence energy landscapes of the end members are visualised to reveal potential sodium-ion transport pathways. A structural threshold is reached for $Na_2Y_{0.5}Nb_{0.5}Cl_6$, revealing a limit for niobium polyhedral distortion while the unit cell volume is retained up to 50% Nb substitution. $Na_2Y_{0.5}Nb_{0.5}Cl_6$ shows the greatest RT ionic conductivity enhancement in the series, from 10^{-11} S cm^{-1} to 10^{-5} S cm^{-1}.

1. Introduction

The demand for energy security underscores the need to improve further battery technologies for long-term energy storage, especially those capable of supporting large-scale, grid-level storage using abundant, inexpensive elements. Lithium-ion batteries have greatly transformed portable electronics, electric vehicles, and the integration of renewable energy grids, helping to address the intermittency issues of solar and wind power. However, the rising demand for lithium and cobalt—key components in this transition—raises concerns about sustainable and ethical sourcing, as well as price volatility driven by their limited natural abundance.[1–4] Sodium-ion batteries have emerged as a promising alternative to lithium-based systems and show compatibility with existing lithium infrastructure. Sodium is among the most prevalent elements in the Earth's crust; its sustainable extraction from both oceanic and terrestrial sources is a vital step toward reducing raw material costs and meeting the global demand for battery technologies.[1,5]

To unlock the full potential of sodium-ion technology, researchers are shifting away from flammable organic liquid electrolytes and toward safer solid-state alternatives. The most common class of solid-state sodium electrolytes are sulphides, oxides, and, more recently, halides. Sodium sulphide electrolytes generally exhibit high ionic conductivity and can operate under mild synthetic conditions, but suffer from a narrow electrochemical stability window and are sensitive to moisture.[6–9] In contrast, while oxide-based electrolytes offer superior thermal and electrochemical stability, their performance is significantly hindered by high grain-boundary resistance, which impedes ion flow at the interface and results in moderate ionic conductivities.[10–14] Among these, sodium halide derivatives are attracting interest as candidates for sodium-ion batteries owing to their excellent interfacial contact with electrodes, broad electrochemical stability windows, defect tolerance, and extensive synthetic versatility, all of which are crucial for efficient ion transport during operation cycling.[15–25] To date, several sodium halide derivatives have been reported with a general framework $Na_nM^{6-n}X_6$ (M = Al^{3+}, Y^{3+}, Sc^{3+}, Ti^{3+}, In^{3+}, Cr^{3+}, Er^{3+}, Eu^{3+}, Lu^{3+}, Zr^{4+}, Hf^{4+}, V^{5+}, Nb^{5+}, Ta^{5+}; X$^-$ = F, Cl, Br, I).[15,17–20,22,26–33] For example, the role of polymorphism and cation disorder in $Na_{3-x}Y_{1-x}Zr_xCl_6$ was studied, and it was found that transition metal ordering influences ionic transport through polyanion rotation at elevated temperatures.[18] A less-researched halide derivative is spinel-type sodium-based electrolytes, Na_2MCl_4 (M = $Y_{2/3}$, $Sc_{2/3}$, *etc.*), which are thought to have high ionic conductivities and a wide electrochemical window; however, these spinel compounds are largely theoretical.[34–36] Analogous lithium halide electrolytes have demonstrated that halide frameworks can overcome some of the limitations described above, offering wide electrochemical stability windows, good compatibility with oxide cathodes, and tuneable ionic conductivities through compositional engineering.[34,37–41] The electrochemical properties of these materials can be improved by tailoring their composition and structural framework through M and X ions and aliovalent substitutions that introduce vacancies *via* cation disorder. In

[a]*Department of Chemistry, University of Alberta, Edmonton, Alberta, T6G 2G2, Canada. E-mail: vladimir.michaelis@ualberta.ca*

[b]*School of Materials Science and Engineering, Nanyang Technological University, 639798, Singapore*

© 2026 The Author(s). Published by the Royal Society of Chemistry

Open Access Article. Published on 26 February 2026. Downloaded on 3/19/2026 5:43:23 PM. This article is licensed under a Creative Commons Attribution-NonCommercial 3.0 Unported Licence.

addition to vacancies, aliovalent substitutions can force the material to undergo phase changes; however, the mechanisms by which ionic conductivity is influenced by these substitutions are not fully understood. Nonetheless, cationic substitution has been shown to improve the ionic conductivity of sodium halide electrolytes to 10^{-4} S cm^{-1}, with the highest non-substituted conductivity reported in $NaTaCl_6$ at 10^{-4} S cm^{-1}.[17,42,43] Hence, further research into aliovalent substitution in solid electrolyte frameworks may be an effective strategy to enhance ionic conductivity relative to their respective end members.[44]

While halide electrolytes are promising, their performance optimisation relies on understanding their atomic structure. Diffraction methods reveal the overall long-range structure, but it is typically the local chemical environment—including disorder, defects, and variations in chemical surroundings—that affects ionic transport. Differences in local environments can significantly affect activation energy barriers and alter sodium diffusion pathways. Solid-state nuclear magnetic resonance (NMR) spectroscopy is a robust analytical technique that provides structural and dynamic information on the impact of aliovalent substitution by probing local and medium-range structural components in ordered and disordered materials. Specifically, ^{23}Na (nuclear spin, $I = 3/2$) NMR is highly sensitive due to its 100% natural abundance, small quadrupole moment (Q = 10.4 fm^2), and moderate chemical shift range. These properties enable one- and two-dimensional NMR methods to analyse various components in batteries, including electrolytes, cathodes and anodes.[45–50] Further extension of the polyanionic structure is accessible by studying the M-site using other NMR-active nuclei, such as ^{25}Mg, ^{27}Al, ^{89}Y, ^{93}Nb, and ^{125}Te.[12,51–59] Therefore, combining insights from both short- and long-range structures is essential for establishing precise structure–property relationships at the nanoscale and advancing the development of solid-state sodium electrolytes.

This study explores the impact of aliovalent niobium substitution in $Na_{3-2x}(Y_{1-x}Nb_x)Cl_6$ on the crystal structure, sodium-ion dynamics, and resulting ionic conductivities. A series of compounds is synthesised using high-energy mechanochemistry and characterised by complementary powder X-ray diffraction (PXRD) and ^{23}Na NMR spectroscopy to elucidate the long- and short-range structural evolutions induced by Y/Nb mixing and their influence on sodium-ion electrochemical properties. Subsequent ^{93}Nb NMR experiments reveal the extent of local octahedral distortion of the $[NbCl_6]^-$ polyanion. Across the series, the nominal $Na_2Y_{0.50}Nb_{0.50}Cl_6$ compound exhibits the highest ionic conductivity with potential Na-ion transport pathways visualised using bond valence sum energy calculations. These findings improve comprehension of the structure and the cation-dynamic role of aliovalent substitution in sodium-containing solid electrolytes based on metal halides.

2. Results and discussion

High-energy mechanochemistry offers an environmentally friendly method to create solid solutions with reduced crystallinity. This is achieved through site disorder and structural distortion, which enhance the ionic conductivity of the material electrolyte.[60,61] This approach was used to synthesise a series of $Na_{3-2x}Y_{1-x}Nb_xCl_6$ compounds, with $x = 0$, 0.10, 0.25, 0.50, 0.75, 0.90, and 1.0, and the structure and ionic properties were characterised by PXRD, NMR, and EIS. Herein, the samples will be referred to as YNb0, YNb10, YNb25, YNb50, YNb75, YNb90, and YNb100, respectively, where the number indicates the percentage of Nb substitution at the Y position in the crystal structure.

2.1 Long-range $Na_{3-2x}Y_{1-x}Nb_xCl_6$ periodic structure

2.1.1 Parent end-members. The crystal structures of the parent end members are shown in Fig. 1a and b. Na_3YCl_6 is reported to have two polymorphs, crystallising in a trigonal space group, $R\bar{3}$, or a monoclinic space group, $P2_1/c$.[18,62] The trigonal polymorph is accessible through low-temperature, slow-cooling synthetic routes, whereas the high-temperature monoclinic polymorph can be obtained through high-energy ball-milling. While both parent phases crystallise in the space group no. 14, $P2_1/c$, Na_3YCl_6 is commonly depicted as $P2_1/n$ such that β is closest to 90° and is related to the Na_3AlF_6 structure type, whereas $NaNbCl_6$ is its own unique structure type. Both end members consist of alternating layers of their respective $[YCl_6]^{3-}$ and $[NbCl_6]^-$ octahedra but differ in their sodium environments. Na_3YCl_6 has two different Na crystallographic sites, Na1 (2b) and Na2 (4e), which are arranged in alternating layers of octahedral and prismatic sites along the *a*-axis, with coordination numbers of six and five, respectively. The octahedral and prismatic Na sites are connected *via* edge- and corner-sharing polyhedra, respectively. In contrast, $NaNbCl_6$ contains only one distinct prismatic Na crystallographic site, Na2 (4e), which occupies every other layer along the *c*-axis.

Na_3YCl_6 and $NaNbCl_6$ can be seen as two members of a broader $Na_nM^{6-n}Cl_6$ series where $n = 1$ (M = Nb) and $n = 3$ (M = Y), shown in Fig. 1c–e. The monoclinic Na-based series also includes a reported $n = 2$ member from Pearson's Crystal Data (PCD), Na_2IrCl_6 (K_2TeBr_6 type, 473 K), and a Na_2ZrCl_6 phase that coexists with its trigonal polymorph, although no structure is reported (no higher members, $n > 3$, have been found). Charge neutrality in the isostructural Na_2IrCl_6 necessitates sodium deficiency with respect to Na_3YCl_6. It is manifested as cation vacancies in the 2b sites, where octahedral Na atoms would otherwise be occupied, like in Na_3YCl_6. To relate $NaNbCl_6$ to its Ir- and Y-bearing counterparts, both the 2b and half of the 4e sites can be imagined to be occupied by Na vacancies. The further removal of half of the 4e sites from Na_2IrCl_6 to $NaNbCl_6$ seems to distort the structure severely, leading to the need for a larger cell to accommodate the new long-range ordering (*e.g.* the ordering of Na and "former" prismatic Na vacant sites) and crystallising with $Z = 4$ formula units (*vs.* $Z = 2$ in the other two structures). Overall, the main structural difference between Na_3YCl_6 and $NaNbCl_6$ is the absence of octahedral and half of the prismatic Na sites, which occurs to maintain charge balance when Y(III) is replaced by Nb(V). The Na vacancy-driven structural relationship described suggests (1) the possible existence of a solid solution between the $n = 1$ and the $n = 3$ structures, in which a structure closely related to Na_2IrCl_6 could be mimicked by a 1 : 1 mixture of the end members, and (2) some degree of

 © 2026 The Author(s). Published by the Royal Society of Chemistry

Open Access Article. Published on 26 February 2026. Downloaded on 3/19/2026 5:43:23 PM.
This article is licensed under a Creative Commons Attribution-NonCommercial 3.0 Unported Licence.

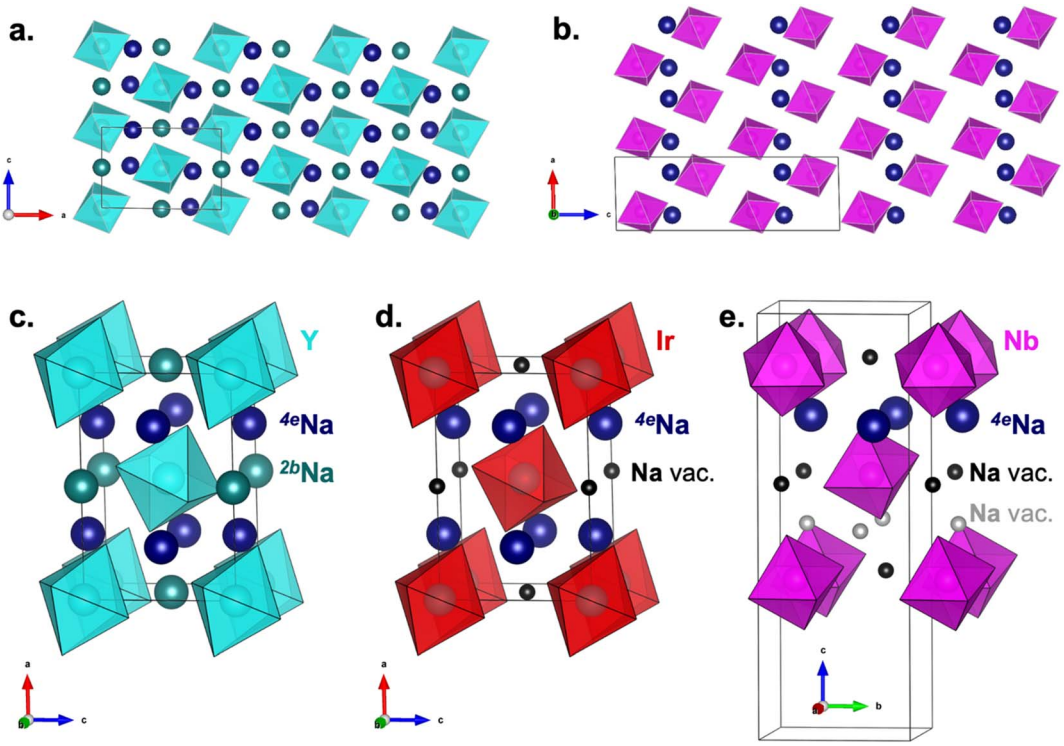

Fig. 1 (a) Supercell of Na_3YCl_6 (space group $P2_1/n$) with Na atoms occupying both octahedral and prismatic environments shown in teal and dark blue, respectively. (b) Supercell of $NaNbCl_6$ (space group $P2_1/c$) with Na atoms occupying only prismatic environments shown in dark blue. Crystal structures of (c) Na_3YCl_6 ($P2_1/n$), (d) Na_2IrCl_6 ($P2_1/n$), and (e) $NaNbCl_6$ (space group $P2_1/c$) are shown in a bbc-like arrangement to emphasise the progressive loss of Na sites (2b and 4e) as the transition-metal oxidation state is increased. The depletion of Na from the 2b and 4e Wyckoff positions is indicated in black and grey spheres, respectively.

chemical control over Na vacancies in a wide range of concentrations.

2.1.2 Aliovalent substitutions. Powder X-ray diffraction was conducted for the YNb series shown in Fig. 2a and used to refine the lattice parameters, Table 1. The PXRD peaks are relatively broad, indicating low crystallinity as expected from the high-energy ball-milling method – the large broad feature around 15° is attributed to mineral oil. Due to the low crystallinity of the compound, the quality of the XRD powder patterns is insufficient to determine atomic positions; however, using Pawley refinement, it is possible to accurately determine the unit cell parameters without being constrained by peak intensities (as required in Rietveld refinement). Therefore, Pawley refinements were conducted on the primary phase, while Rietveld refinement was employed to analyse the NaCl impurity peaks, thereby constraining the peak intensities to prevent fitting of the NaCl peaks to the main phase, particularly because the strongest NaCl peaks overlap with those of the main phase. As Nb content increases in the YNb substituted series, peak positions shift towards larger 2θ, consistent with the smaller ionic radius of Nb^{5+} (0.64 Å) compared to Y^{3+} (0.9 Å) in a six-member coordination environment.[63] To better compare how Nb content alters the unit cell, Fig. 2b displays the change in formula unit volume since Na_3YCl_6 contains two formula units, whereas $NaNbCl_6$ has four formula units. The unit cell shrinks from YNb0 to YNb50; however, the volume remains relatively the same until it reaches a critical threshold above YNb50. Once Nb loading exceeds 50%, a drastic change in the unit cell occurs, as seen for YNb90 and YNb100, dropping from approximately 250 to 210 Å^3. Unfortunately, the limited resolution of the PXRD patterns for YNb75 prevented refinement of this structure, so it was not included in the plot. To enhance the understanding of the local structural changes, solid-state ^{23}Na and ^{93}Nb NMR spectroscopy was conducted.

2.2 Influence of aliovalent substitution on local sodium structure and dynamics using ^{23}Na NMR spectroscopy

2.2.1 ^{23}Na chemical structure. The ^{23}Na NMR spectra shown in Fig. 2c reveal two different sodium chemical environments for YNb0 and a single environment for YNb100, consistent with their crystal structures. The YNb100 resonance appears at a centre of gravity shift (δ_{cgs}) of −9.4 ppm and is attributed to the prismatic Na site. In the YNb0 sample, the prismatic site is seen with an isotropic chemical shift (δ_{iso}) of −7.4 ppm and a second-order quadrupolar lineshape due to a quadrupole coupling constant, C_Q, of 1.0(3) MHz. GIPAW-DFT computations (see Fig. S1 and Table S1) predict that the prismatic site possesses a sizable C_Q of 1.3 MHz. For simplicity, the δ_{cgs} for the prismatic site in YNb0 will be used below and is reported as −9.1 ppm. This leaves the resonance at δ_{cgs} = 3.2 ppm attributed to the octahedral Na sites with negligible second-order quadrupolar broadening. Residual amounts (<1%) of the competing $R\bar{3}$ phase can be observed between 2 and −1 ppm.[64] The resonance at 7.2 ppm coincides with unreacted NaCl – a common impurity in Na_3YCl_6

Open Access Article. Published on 26 February 2026. Downloaded on 3/19/2026 5:43:23 PM.
This article is licensed under a Creative Commons Attribution-NonCommercial 3.0 Unported Licence.

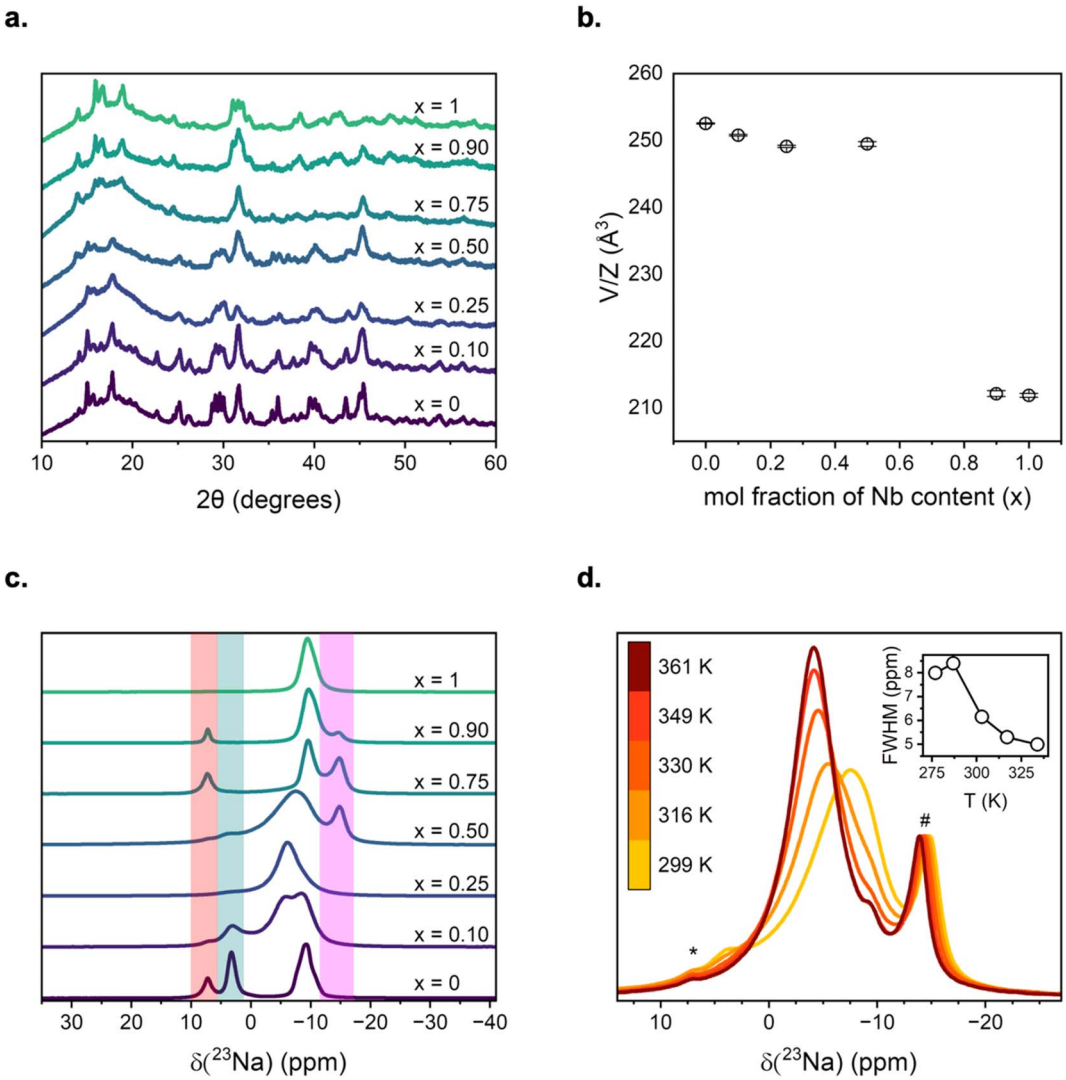

Fig. 2 (a) Powder X-ray diffraction pattern of YNb series. (b) Plot of volume per formula unit as a function of nominal Nb substitution. Data point for YNb75 excluded from the plot because powder pattern refinement was unsuccessful. (c) ^{23}Na MAS NMR spectra ($B_0 = 11.7$ T, $\nu_{rot} = 10$ kHz) for YNb; red bar indicates region of NaCl impurity, teal bar denotes octahedral Na site, and magenta bar highlights region of $NaNbO_xCl_{6-2x}$ impurities. (d) VT ^{23}Na MAS NMR spectra ($B_0 = 11.7$ T, $\nu_{rot} = 10$ kHz) of YNb50 collected at different temperatures. Asterisk (*) indicates NaCl impurity and hash (#) indicates $NaNbO_xCl_{6-2x}$ impurity. (inset) Plot of full width at half maximum (FWHM) as a function of temperature.

systems due to its unreactive nature and the propensity of YCl_3 to stick to the walls of the ball-mill jar during synthesis.[60,64,65] Upon 10% substitution of Nb into the sample (YNb10), there is an emergence of a new ^{23}Na peak with a δ_{cgs} of −6 ppm that is tentatively assigned to the sodium chemical environments interacting with both $[NbCl_6]^-$ and $[YCl_6]^{3-}$ octahedra. The octahedral sites are observed in the ^{23}Na NMR spectra up to YNb50, consistent with PXRD data, suggesting a single phase with the Na_3YCl_6 unit cell volume. Likewise, three Na sites remain up to YNb50, where the ∼−6 ppm and prismatic

Table 1 Unit cell parameters for $Na_{3-2x}Y_{1-x}Nb_xCl_6$ series[a]

Sample	Space group	V (Å^3)	a (Å)	b (Å)	c (Å)	β (°)
Na_3YCl_6 (YNb0)	$P2_1/n$	505.1(1)	10.145(2)	7.257(1)	6.860(1)	90.79(2)
$Na_{2.8}Y_{0.90}Nb_{0.10}Cl_6$ (YNb10)	$P2_1/n$	501.6(2)	10.117(3)	7.248(2)	6.841(1)	90.86(2)
$Na_{2.5}Y_{0.75}Nb_{0.25}Cl_6$ (YNb25)	$P2_1/n$	498.3(3)	10.105(4)	7.227(3)	6.823(2)	91.01(2)
$Na_2Y_{0.50}Nb_{0.50}Cl_6$ (YNb50)	$P2_1/n$	498.9(7)	10.124(1)	7.267(7)	6.791(4)	91.16(5)
$Na_{1.5}Y_{0.25}Nb_{0.75}Cl_6$ (YNb75)	$P2_1/c$	n.d.	n.d.	n.d.	n.d.	n.d.
$Na_{1.2}Y_{0.10}Nb_{0.90}Cl_6$ (YNb90)	$P2_1/c$	849(1)	6.414(7)	6.905(8)	19.16(1)	90.96(7)
$NaNbCl_6$ (YNb100)	$P2_1/c$	847(1)	6.411(5)	6.911(6)	19.13(1)	90.88(3)

[a] n.d. – not determined.

 © 2026 The Author(s). Published by the Royal Society of Chemistry

Open Access Article. Published on 26 February 2026. Downloaded on 3/19/2026 5:43:23 PM.
This article is licensed under a Creative Commons Attribution-NonCommercial 3.0 Unported Licence.

resonances coalesce with small residual octahedral sites at 3.2 ppm for the YNb25 and YNb50 compounds. This coalescence is partly due to the averaging of the Na chemical environments during Na exchange, which appears to be at least on the millisecond time scale, *vide infra*, and to sensitivity to changes in the unit cell volume and to the influence of Y/Nb next-nearest neighbours. Upon equimolar mixing of Y and Nb, YNb50 reveals the broadest resonance attributed to the random disorder of $[NbCl_6]^-$ and $[YCl_6]^{3-}$ polyanions, inducing a large distribution of sodium chemical environments. YNb50 appears to be the critical threshold for three *vs.* one sodium sites, as higher Nb loading results in only a single prismatic site being resolved, consistent with the change in unit cell volume observed in XRD analysis.

Above 50% Nb substitution, a new resonance emerges at δ_{cgs} of −14.7 ppm and is attributed to the formation of an oxychloride impurity, $NaNbO_xCl_{6-2x}$ (<15%), that is amorphous in nature. The chemical shift varies slightly across literature reports, and its range is shown in Fig. 2c (magenta). The variance in chemical shift is due to the tendency of Nb-rich phases to oxidise, forming a mixed anion phase; however, further refinement and elemental analysis are not possible due to the poor crystallinity and short coherence lengths.[66–69] An attempt to form $NaNbOCl_4$ is made; the PXRD and ^{23}Na NMR are shown in Fig. S2. The main oxychloride resonance is observed close to the prismatic site for YNb100 at $\delta_{cgs} = -9.8$ ppm, but smaller resonances are observed towards even lower frequency and are attributed to $NaNbO_xCl_{6-2x}$.

2.2.2 Sodium-ion dynamics. Variable-temperature (VT) 1D and 2D ^{23}Na NMR spectroscopy were performed to improve our understanding of sodium-ion dynamics in these aliovalent solid electrolytes. Nuclear spin–lattice relaxation (T_1) times were measured to assess the associated activation energies collecting results from 299 to 361 K. These results were analysed with the Arrhenius plot (Fig. S3) revealing our analysis is limited due to being on the low temperature flank ($\omega_0 \times \tau_{NMR} \gg 1$), where ω_0 is the angular Larmor frequency and τ_{NMR} is the correlation time. An analysis of the Arrhenius behaviour reveals local activation energies for Na on the order of 0.02–0.20 eV (Table S2). The extracted activation energies do not imply fast sodium-ion diffusion but rather local vibrations, local cation exchange, or the influence of unit-cell expansion/contraction. Due to hardware limitations, higher temperatures could not be reached, thereby restricting further analysis. Fig. 2d shows the ^{23}Na VT MAS NMR for YNb50 up to 361 K. Coupled with lower symmetry in the first coordination sphere (prismatic), the broad resonance from ^{23}Na NMR data suggests a distribution of Na environments with neighbouring $[NbCl_6]^-$ and $[YCl_3]^{3-}$ octahedra surrounding Na in the second coordination sphere. The ^{23}Na chemical shift for YNb50 becomes increasingly sharp with elevated temperature, supporting the presence of Na dynamics such as chemical exchange or random motion, thereby alleviating residual anisotropic interactions. Additionally, the octahedral resonance at 3.2 ppm decreases and exchanges with the new resonance. Similarly, ^{23}Na VT NMR of YNb10 and YNb25 (Fig. S4) supports motional averaging, as the octahedral site at 3.2 ppm coalesces with the main resonance at 349 K and 316 K, respectively. The prismatic site for YNb10 also coalesces at 349 K. These results reveal that local exchange between different sodium sites is activated by increased thermal energy. The absence of coalescence in YNb0 up to 316 K (Fig. S4) implies that either no Na-ion exchange occurs in this parent phase, or it is too slow to influence the NMR spectra. While examination of the 1D spectra provides evidence that Na-ion exchange occurs with increasing Nb loading, two-dimensional exchange spectroscopy (EXSY) experiments were performed to determine whether further spectroscopic evidence of slow Na-ion dynamics occurs in the resolved Y-rich phases (YNb0 and YNb10).

2.2.3 Sodium chemical exchange. Two compounds exhibit good chemical-shift resolution for two Na-sites in YNb0 and three Na-sites in YNb10, enabling 2D ^{23}Na EXSY NMR to investigate the degree of sodium-ion exchange further. VT 2D EXSY NMR on YNb0 enables the Na-ion jump rate and activation energy between the octahedral and prismatic Na environments to be determined using a series of mixing times (τ_{mix}). Analysis of the T_1 values was performed at each prescribed temperature point to ensure that $\tau_{mix} < T_1$. If mixing times are too short, only the diagonal (absence of cross-peaks) is recorded; mixing times longer than T_1, however, allow spin–lattice relaxation effects to dominate, so that the cross-peak intensities are no longer representative of chemical exchange.[70] Fig. 3a represents YNb0 with a $\tau_{mix} = 500$ ms, where the spectrum reveals no cross-peak intensities between the two Na environments at room temperature. Cross-peak intensity emerges on the sample when the mixing time is increased to 1.5 s (Fig. 3b), representing chemical exchange between the two sites. This result indicates that the octahedral and prismatic sites do exchange, however, very slowly, on the order of seconds. To form the buildup curves, cross-peak intensities are normalised to the sum of the diagonal peaks and plotted as a function of mixing time at each prescribed temperature (308 K, 316 K, and 325 K). Ideally, a plateau should be observed with increased mixing times; however, maximal cross-peak intensities are unachievable at the probed temperatures, as longer mixing times violate the measured T_1 times. The Na-ion hopping or jump rate, k, is determined by fitting the buildup curves (Fig. 3d) with a first-order exponential function to yield 3.2(3), 1.1(7), and 0.6(1) s^{-1} at 308 K, 316 K, and 325 K, respectively. At 297 K, the Na dynamics were too sluggish to produce a satisfactory buildup curve while ensuring $\tau_{mix} < T_1$. Two-dimensional EXSY NMR data at 297 K are therefore omitted from the buildup curve and activation energy analysis. The activation energies (E_a) for Na-ion hopping can be determined through an Arrhenius analysis using the equation:

$$k = Ae^{-E_a/RT} \tag{1}$$

where A is the pre-factor, R is the ideal gas constant, and T is the temperature. Fig. 3e reveals an activation energy of 0.84 eV required for local Na-ion hopping in YNb0. The ^{23}Na EXSY NMR for YNb10 was used to qualitatively assess if the new resonance at −6 ppm is involved in chemical exchange with the former octahedral and prismatic sites. As shown in Fig. 3c, with

Open Access Article. Published on 26 February 2026. Downloaded on 3/19/2026 5:43:23 PM.
This article is licensed under a Creative Commons Attribution-NonCommercial 3.0 Unported Licence.

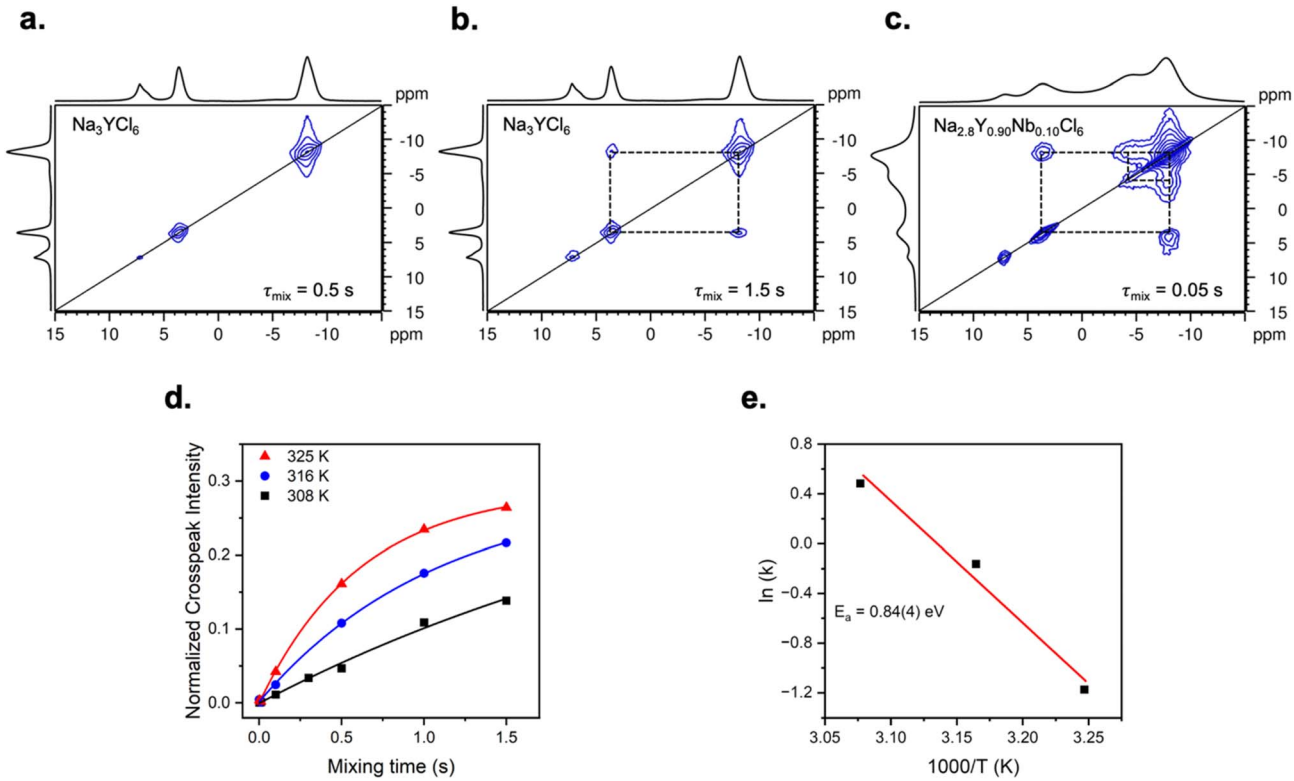

Fig. 3 ^{23}Na EXSY NMR spectra ($B_0 = 18.8$ T, $\nu_{rot} = 10$ kHz) of YNb0 at 297 K at different mixing times (a) 0.5 s and (b) 1.5 s, and (c) YNb10 at 290 K with $\tau_{mix} = 0.05$ s. Corresponding 1D spectra are projected on the left and top of the 2D spectra. The diagonal peak at 7.2 ppm is NaCl impurity. (d) Buildup curves of YNb0 normalised cross-peak intensities as a function of mixing times sampled at three different temperatures. (e) Arrhenius plot of local Na-ion hopping rates derived from the buildup curves as a function of 1000/*T*.

a mixing time of only 50 ms, cross peaks appear between the octahedral and prismatic sites and between the prismatic and new Na site. However, there does not appear to be any chemical exchange occurring between the octahedral site and the new Na site. This finding indicates two outcomes: that Nb substitution initiates faster room-temperature Na-ion exchange (ms *vs.* s timescales) and that this new phase has three distinct Na chemical environments that all participate in exchange across the material, yet selectively with one another. Further analysis to assess the jump rate and activation energies was not possible due to overlapping NMR resonances, which inhibited a detailed analysis similar to that done for YNb0. Finally, to ensure the competing $R\bar{3}$ phase does not influence the main $P2_1/n$ phase, an EXSY experiment at 325 K and a maximum mixing time shows no cross-peaks between the two phases (*i.e.* the $R\bar{3}$ phase does not contribute to the dynamics of the main phase), consistent with a previous report.[64] Likewise, the residual NaCl peak at 7.2 ppm shows no cross peaks with the main phase and therefore does not contribute to Na-ion exchange.

2.3 Influence of aliovalent substitution on local niobium environments using ^{93}Nb NMR

^{93}Nb is a sensitive quadrupolar nucleus ($I = 9/2$) found in 100% natural abundance with a large quadrupole moment ($Q = -32.0$ fm^2). While 100% abundance is highly advantageous, the quadrupolar moment often leads to significant second-order quadrupole broadening of the central transition. ^{93}Nb NMR spectra were collected at 11.7 and 18.8 T under both spinning and non-spinning conditions to allow for accurate fitting of the NMR parameters. Fig. 4 shows the ^{93}Nb NMR of the series synthesised in this work. The second-order quadrupole interaction in ^{93}Nb NMR cannot be ignored even at high magnetic fields and under MAS conditions, Fig. 4b. Nonetheless, the quadrupole coupling constant is manageable at conventional magnetic field strengths used here for Nb-rich compounds. Table 2 contains the NMR parameters for the series, and the corresponding NMR simulations are shown in Fig. 4b–d and S5. Contrary to a previous report[67] stating a 100 MHz C_Q for $NaNbCl_6$, the C_Q of the same sample synthesized in this work is only 10.2(3) MHz with δ_{iso} of 30 ppm and a sizeable chemical shift anisotropy (Ω) of 160 ppm that dominates the central transition lineshape at 18.8 T. Our experimental findings were simulated at 9.4, 11.7 and 18.8 T solving for a unique fit. For comparison, the previously reported C_Q of 100 MHz would result in a central transition spanning 3600 ppm at 9.4 T (Fig. S6), which does not agree with their published NMR spectra. Across the series, ^{93}Nb NMR data reveal similar local Nb environments from YNb100 to YNb50 with approximately a 1 MHz increase in C_Q as Nb is replaced with Y. That is, the Nb environment does not seem to be heavily distorted from 100 to 50% Nb content. This finding complements the ^{23}Na NMR and PXRD data, which only show minor changes.

 © 2026 The Author(s). Published by the Royal Society of Chemistry

Open Access Article. Published on 26 February 2026. Downloaded on 3/19/2026 5:43:23 PM.
This article is licensed under a Creative Commons Attribution-NonCommercial 3.0 Unported Licence.

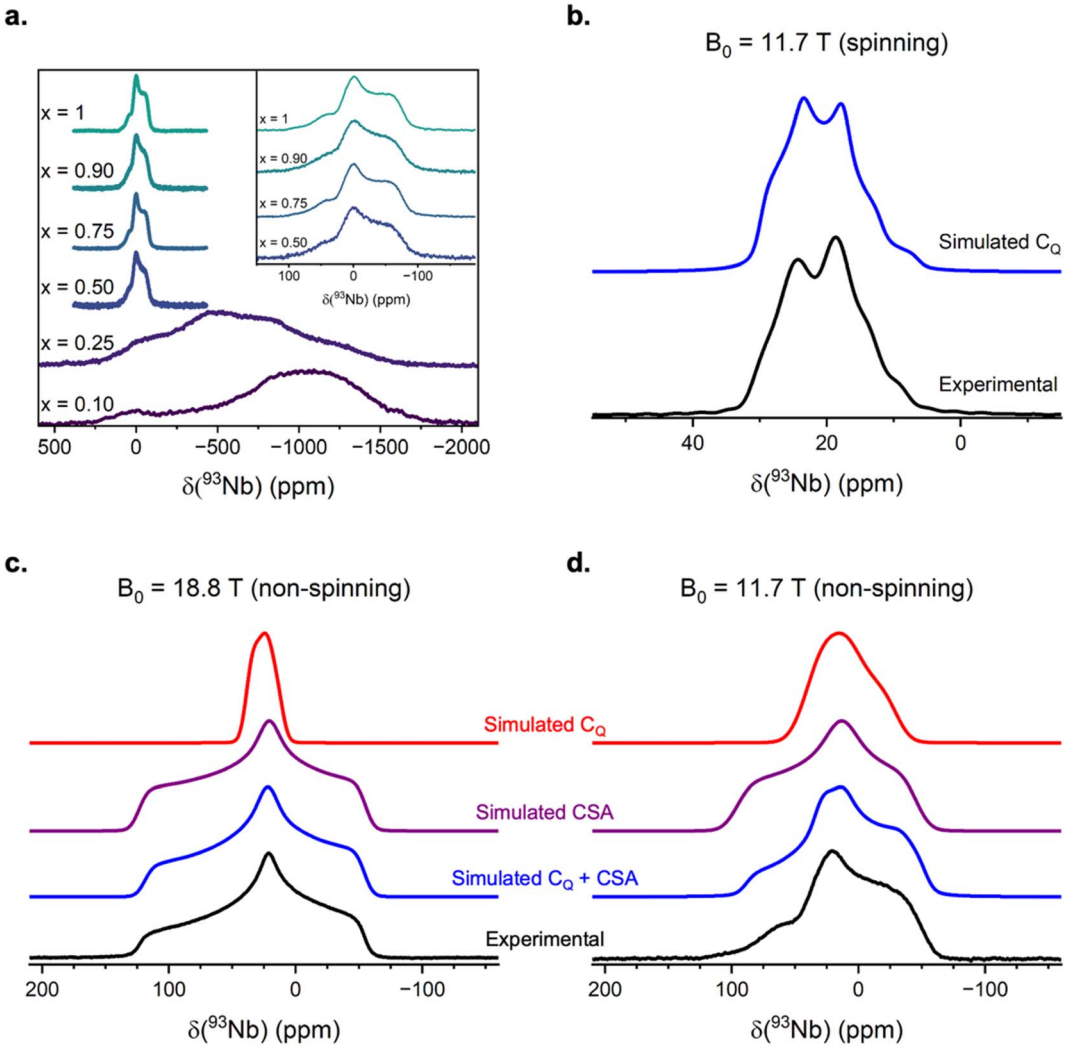

Fig. 4 (a) Non-spinning ^{93}Nb NMR spectra collected at two different magnetic fields, $B_0 = 18.8$ T ($x = 0.10$ and 0.25) and $B_0 = 11.7$ T ($x = 0.50$ to 1). (inset): Magnification of samples from $x = 0.50$ to 1 for enhanced clarity. ^{93}Nb NMR spectra of $NaNbCl_6$ with experimental (black), simulated C_Q and CSA contributions (blue), simulated CSA contributions (purple), and simulated C_Q (red) at: (b) 11.7 T (MAS, $\nu_{rot} = 10$ kHz), (c) 18.8 T (non-spinning), (d) 11.7 T (non-spinning).

As the niobium-rich compounds transition to yttrium-rich phases (<50% Nb), $[NbCl_6]^-$ polyhedra appear to be heavily strained as a drastic change in the ^{93}Nb central transition occurs, revealing a sizable second-order quadrupolar broadened central transition spanning over 500 ppm. While the exact cause of this is presently unknown, the M–Cl bond distances may provide some insight. Using crystal structure information derived from the parent phases, it is determined

Table 2 Experimental ^{93}Nb NMR parameters for $Na_{3-2x}Y_{1-x}Nb_xCl_6$, $NaNbO_xCl_{6-2x}$, and other reported niobium compounds

Sample	C_Q (MHz)	η	δ_{iso} (ppm)	Ω (ppm)	κ	α (°)	β (°)	γ (°)
$NaNbCl_6$	10.2(3) [11.1]^a	0.47(1) [0.67]^a	30(2)	160(20)	−0.16(2)	69(5)	25(5)	28(5)
$Na_{1.2}Y_{0.10}Nb_{0.90}Cl_6$	10.5(5)	0.72(5)	21(2)	140(10)	0.00	83(5)	24(5)	10(5)
$Na_{1.5}Y_{0.25}Nb_{0.75}Cl_6$	10.6(5)	0.72(5)	21(2)	136(10)	0.00	79(5)	24(5)	6(5)
$Na_2Y_{0.50}Nb_{0.50}Cl_6$	11.6(5)	0.57(5)	25(2)	142(10)	−0.21(2)	78(5)	23(5)	15(5)
$Na_{2.5}Y_{0.75}Nb_{0.25}Cl_6$	69.4(5)	0.52(5)	−432(10)	522(30)	0.67(4)	18(5)	62(5)	49(5)
$NaNbO_xCl_{6-2x}$	80(5)	0.15(5)	−541(50)	—	—	—	—	—
$YNbO_4$ (ref. 72)	82.2	0.38	−840	307	−0.49	−1	17	95
Na_5NbO_5 (ref. 73)	11.1	0.01	−903	144	−0.33	—	—	—
$NaNbO_3$ (ref. 74)	22.7	—	−1073	—	—	—	—	—
H-Nb_2O_5 (ref. 75)	24	—	−1204	—	—	—	—	—

^{a} Computed GIPAW-DFT values from CASTEP.

Open Access Article. Published on 26 February 2026. Downloaded on 3/19/2026 5:43:23 PM.
This article is licensed under a Creative Commons Attribution-NonCommercial 3.0 Unported Licence.

that the M–Cl bond distances differ significantly between the end members and may be inducing local- and medium-range distortions. Y–Cl bond distances are in a narrow range, varying from 2.62 to 2.63 Å, compared to Nb–Cl bond distances that are larger in range but more tightly packed, spanning from 2.25 to 2.48 Å. Although isolated, the Y-rich crystal structure will expand and require Na octahedral sites to return to maintain charge balance associated with replacing Nb^{5+} with Y^{3+}. In addition, the ionic-covalent character of the different polyanions may also be impacted by higher Y^{3+} substitution.[71] The observed reduction in sensitivity (signal-to-noise) of the Y-rich compounds (YNb10 and YNb25) in the NMR spectra is due to a combination of lower Nb concentration and the formation of a large quadrupole coupling constant of 69 MHz (Fig. S5). Finally, the chemical shift is also heavily influenced, shifting to lower frequency, to a δ_{iso} of −432 ppm for YNb25, for example. This result suggests that the stability of Y-rich phases may be more susceptible to oxidation of the niobium chemical environment. To further assess this possibility, we examine the synthesised sodium niobium oxychloride more closely.

2.4 Niobium oxychloride and niobate species

The observed ^{93}Nb NMR chemical shifts for YNb25 and YNb10 lie between those of Nb-rich sodium chloride phases and other niobate species, where earlier studies on niobium oxide compounds typically report isotropic chemical shifts between −400 and −1600 ppm and are sensitive to their coordination environment.[58,59,72–77] While our experimental observation suggests the formation of an oxychloride species, with an isotropic chemical shift found between the chloride and oxide-containing species, the ^{23}Na NMR results (above) do not reveal any formation of a sodium-containing oxychloride (or oxides) in these two Y-rich compounds. Further work is needed to determine precisely how Y concentrations influence the Nb environment and the potential role of vacancies, polyanion disorder and oxidation in these solids. However, our assertion is further confirmed by ^{93}Nb NMR (Fig. 5), where the chemical shifts and C_Qs of known sodium niobate and niobium oxide species do not agree with our experimental data.[72–75] Interestingly, the NMR spectrum of the sodium oxychloride, $NaNbO_xCl_{6-2x}$, synthesised here, and that of yttrium niobate,[72] $YNbO_4$ (which excludes sodium), share some resemblance with our series. As such, the unique ^{93}Nb NMR spectra may be caused by a Y^{3+} substitutional defect for the $[NbCl_6]^-$ polyanion species, serving as an intermediary for the octahedral sodium site – their respective ionic sizes are less than 15% different, Y^{3+} (0.9 Å) *vs.* Na^+ (1.02 Å). Finally, the ^{23}Na NMR results confirm that a minor sodium oxychloride impurity is present in the Nb-rich compounds; however, it accounts for less than 15% of the total sample, which is a low % and, coupled with the large 80 MHz C_Q, is unlikely to be significant. This prevents us from detecting any Nb signal related to this phase. While ^{93}Nb NMR appears to be a sensitive probe nucleus for these types of chemical problems, further exploratory studies are needed into this emerging class of mixed anionic systems.

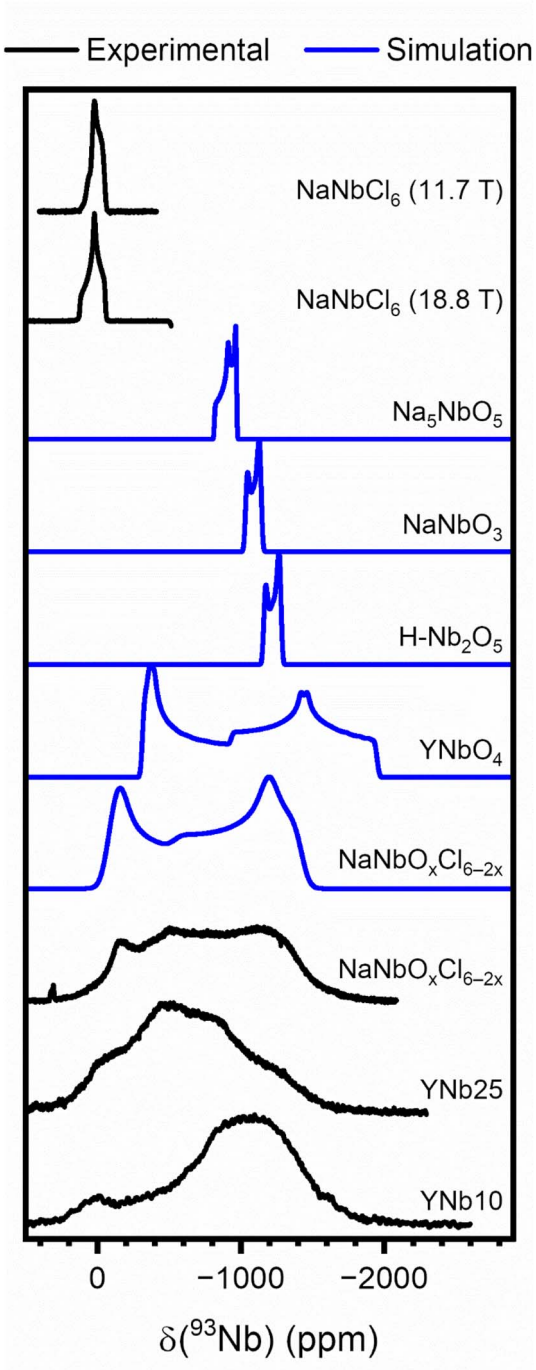

Fig. 5 ^{93}Nb NMR of samples synthesised in this work (black) compared to reported niobium oxides and niobates simulated in blue. The parameters used for simulations are listed in Table 2.

2.5 Ionic conductivity of aliovalent substituted sodium metal halides

Electrochemical impedance spectroscopy (EIS) was performed on the series at temperatures ranging from 304 to 344 K to determine how their unique compositions and structures influence the bulk ionic conductivity of these sodium metal chlorides. The ionic conductivities (σ) were extracted from the Nyquist plots (Fig. 6a and S7) using Ohm's law

 © 2026 The Author(s). Published by the Royal Society of Chemistry

Open Access Article. Published on 26 February 2026. Downloaded on 3/19/2026 5:43:23 PM.
This article is licensed under a Creative Commons Attribution-NonCommercial 3.0 Unported Licence.

$$\sigma = \frac{d}{R \times A} \quad (2)$$

where d is the thickness of the pellet, R is the resistance, and A is the surface area of the pellet. Fig. 6b shows the ionic conductivities as a function of Nb substitution and is tabulated in Table 3. From the end members, ionic conductivities increase exponentially until a maximum is reached for YNb50, yielding 9.0×10^{-5} S cm^{-1} at room temperature. This constitutes an increase by six orders of magnitude from Na_3YCl_6 and one order of magnitude higher than $NaNbCl_6$. From the subsequent VT EIS measurements, the bulk activation energies can be extracted from an Arrhenius-like analysis shown in Fig. 6c. The activation energies range from 0.28 to 0.90 eV, representing the changes in sodium-ion diffusion within the bulk polycrystalline materials.

Table 3 Activation energies extracted from EIS, and ionic conductivities of $Na_{3-2x}Y_{1-x}Nb_xCl_6$ series

Sample	E_a EIS (eV)	σ (S cm^{-1})
Na_3YCl_6 (YNb0)	0.90(1) 0.84(4)[a]	6.1×10^{-11}
$Na_{2.8}Y_{0.90}Nb_{0.10}Cl_6$ (YNb10)	0.39(3)	5.7×10^{-8}
$Na_{2.5}Y_{0.75}Nb_{0.25}Cl_6$ (YNb25)	0.44(5)	2.7×10^{-6}
$Na_2Y_{0.50}Nb_{0.50}Cl_6$ (YNb50)	0.28(9)	9.0×10^{-5}
$Na_{1.5}Y_{0.25}Nb_{0.75}Cl_6$ (YNb75)	0.31(0)	6.0×10^{-5}
$Na_{1.2}Y_{0.10}Nb_{0.90}Cl_6$ (YNb90)	0.29(0)	2.3×10^{-5}
$NaNbCl_6$ (YNb100)	0.35(2)	3.4×10^{-6}
$NaNbO_xCl_{6-2x}$	n.d.	5.0×10^{-4}

[a] Activation energy determined from variable temperature ^{23}Na EXSY NMR.

2.6 Bridging chemical structure, sodium mobility and electrochemical properties

2.6.1 Bond valence energy landscapes. To better understand and visualise the possible Na-ion migration pathways in these solids, Fig. 7 shows a bond-valence energy landscape calculation. The isosurfaces shown are derived from the E_a obtained from EIS measurements, and the migration pathways illustrate the bond-valence energy landscapes calculated with softBV.[78] The predicted E_a for Na_3YCl_6 is underestimated by ~0.32 eV and overestimated by ~0.30 eV for $NaNbCl_6$. Typically, activation energies are overestimated because the program assumes ideal, defect-free crystal structures; however, the higher experimental E_a observed for Na_3YCl_6 can ironically be attributed to the material's disordered nature, which weakens the inductive effect, *vide infra*. Nonetheless, the energy landscapes still provide insight into the dynamics and transport pathways of Na^+ ions within these solids.

Bond valence energy landscape calculations reveal several interstitial sites and saddle points. Briefly, interstitial sites are void spaces that represent a local minima, and saddle points are the transition states or hopping trajectory between two local minima. From the interstitial sites and saddle points, the Na-ion migration pathway for Na_3YCl_6 indicates a 2D diffusion network. A wide zigzag pattern, Na1-s1-Na0 to Na0-s2-i1-s3-Na1, is shown in Fig. 7b. Although Na1-s4-Na0 is shown as a potential migration pathway, it is not expected to be a primary pathway because s4 has a higher energy barrier (0.72 eV) than s1 (0.56 eV) for Na1-s1-Na0. Furthermore, s4 resides between edge-sharing octahedra, but s1 lies on the face of the octahedral Na. Assuming no vacancies in the structure, Na-ion migration between edge-sharing octahedra is clearly unfavourable even though the distance between Na1 and Na0 is shorter, 3.89 Å, than migration through s1, 4.14 Å. A 1D square zigzag pattern, Na0-s1-i1-s2-i2-Na0, is predicted for $NaNbCl_6$ Na-ion migration along the *a*-axis shown in Fig. 7d. The migration barrier is predicted to be higher than Na_3YCl_6, 0.65 *vs.* 0.58 eV, but the opposite is observed experimentally. Incorrect prediction results can be due to 1D diffusion pathways being less efficient than 2D pathways, inductive effects (see below), and the inability to account for the role of vacancies. The bond valence energy landscapes here provide a first approximation for visualising the Na-ion diffusion network but require further

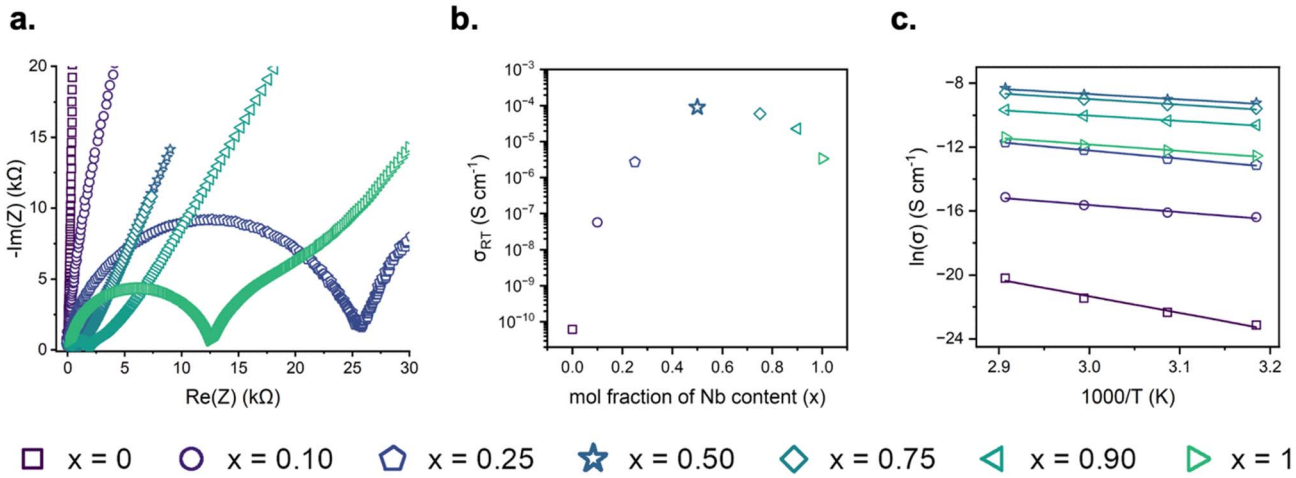

Fig. 6 (a) Nyquist plot of room temperature electrochemical impedance measurements. (b) Ionic conductivities of the YNb series as a function of increasing Nb substitution. YNb50 is bolded to denote that the sample has the highest measured ionic conductivity from the series. (c) Arrhenius plot of ionic conductivities as a function of 1000/T. The reader can refer to the legend below the plots for the sample composition.

Open Access Article. Published on 26 February 2026. Downloaded on 3/19/2026 5:43:23 PM.
This article is licensed under a Creative Commons Attribution-NonCommercial 3.0 Unported Licence.

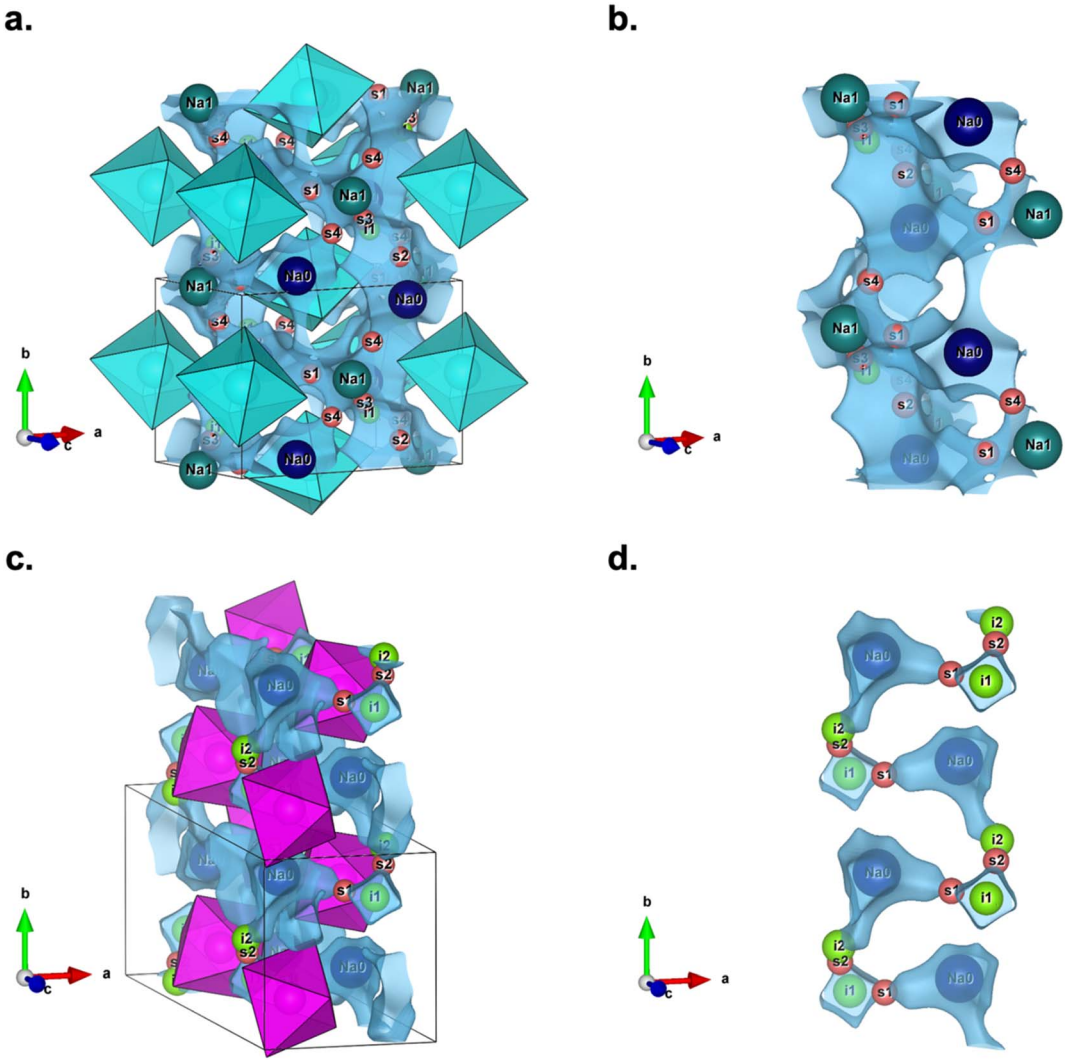

Fig. 7 Bond valence energy landscape of (a) Na_3YCl_6 (isosurface value = 0.90 eV) and (b) closeup of the corresponding potential Na^+ diffusion pathway with $[YCl_6]^{3+}$ omitted for clarity. Similarly, the bond valence energy landscape of (c) $NaNbCl_6$ (isosurface value = 0.35 eV) and (d) a close-up of the corresponding potential Na^+ diffusion pathway with $[NbCl_6]^-$ for clarity. Blue isosurface depicts the Na^+ migration, where yellow denotes interstitial sites, and red denotes saddle points. The chlorines are omitted for clarity.

justification to account for the experimental deviation from the predicted energy barriers, as this model cannot capture local disorder or the increased vacancies induced by ball milling.

2.6.2 Inductive effects. In 1989, Goodenough demonstrated that inductive effects play a role in the overall cationic dynamics, whereby bonding interactions with the anion can modulate the cations' energy landscape.[79] The concept has since been used to explain some phenomena related to solid-state electrolytes.[80] In 2020, Culver *et al.* demonstrated an inductive effect in the lithium superionic conductor $Li_{10}Ge_{1-x}Sn_xP_2S_{12}$.[81] They describe how the electronegativity difference between Ge (2.01) and Sn (1.96) accounts for the reduced ionic conductivity in $Li_{10}SnP_2S_{12}$. That is, the lower electronegativity of Sn leads to a weaker Sn–S–Li bond than the Ge–S bond, resulting in a larger charge density on the S atom. The increase in charge density leads to a stronger coulombic attraction between the S atom and nearby Li cations, thereby strengthening the S–Li bond and increasing the energy barriers to Li-ion migration. In the context of this work, the inductive effect explains the difference in ionic conductivity observed between Na_3YCl_6 and $NaNbCl_6$ but cannot fully account for the series, suggesting that additional effects are influencing these materials (such as structural disorder, Na vacancies, rotation, *etc.*). As expected, the differences in electronegativity between Y (1.22) and Nb (1.6) result in longer Y–Cl bonds (2.62–2.63 Å) than Nb–Cl bonds (2.25–2.48 Å). Additionally, the disordered nature of the materials caused by high-energy ball-milling distorts the $[YCl_6]^{3-}$ octahedra, resulting in deviations from octahedral symmetry, which can lengthen Y–Cl bonds. The increased coulombic interaction between Na–Cl bonds in Na_3YCl_6 should translate into a higher energy barrier required for Na-ion hopping than in $NaNbCl_6$. This is experimentally confirmed: Na_3YCl_6 has an E_a of 0.90 eV, nearly three times larger than $NaNbCl_6$ (0.35 eV). Unfortunately, the inductive effect does not hold across the series presented in this work. That is, while it can explain the

 © 2026 The Author(s). Published by the Royal Society of Chemistry

Open Access Article. Published on 26 February 2026. Downloaded on 3/19/2026 5:43:23 PM.
This article is licensed under a Creative Commons Attribution-NonCommercial 3.0 Unported Licence.

difference between the end members, there is no obvious linear trend of the activation energies as a function of Nb content.

2.6.3 Polyanion rotation. The idea of polyanion rotation is proposed to play an important role in the observed high ionic conductivities.[37,67,82–87] Cation dynamics are said to be influenced by a paddle-wheel effect whereby the rotational mode of anionic polyhedra "push" the cation (Na^+/Li^+) along its migration pathway. Wu *et al.* observe the first instance of polyanion rotation in halide solid-state electrolytes.[29] Through AIMD simulations, the authors note that while the Cl^- is relatively static in Na_3YCl_6, it moves considerably in $Na_{2.25}Y_{0.25}Zr_{0.75}Cl_6$, indicating $[YCl_6]^{3-}/[ZrCl_6]^{2-}$ octahedral rotation. Within our framework, we can assume that YNb0 maintains nearly identical properties to those observed in the aforementioned study, with some variance due to synthetic strategies. With increased Nb substitution, the unit cell remains similar from YNb0 to YNb50 as described earlier, but the larger $[YCl_6]^{3-}$ are replaced with smaller $[NbCl_6]^-$ octahedra. Since YNb50 maintains the larger unit cell volume of YNb0, the smaller $[NbCl_6]^-$ has more space to participate in polyanion rotation along with $[YCl_3]^{3-}$ octahedra at elevated temperatures. The behaviour is expected to be similar to the work by Wu *et al.*[29] where the polyanion rotations become more rigid near room temperature conditions as they are not superionic conductors – YNb50 possesses a slightly higher ionic conductivity than $Na_{2.25}Y_{0.25}Zr_{0.75}Cl_6$, 9.0×10^{-5} S cm^{-1} *vs.* 6.6×10^{-5} S cm^{-1}, respectively. The EIS results lend further support to the faster Na-ion dynamics observed in YNb50, which has the lowest E_a in the series at 0.28 eV. The low E_a indicates low energy barriers for both local and bulk Na-ion dynamics, while ^{23}Na NMR supports a large distribution of sodium chemical environments. While experimental evidence is needed to confirm the extent of polyanion rotation, the situation and the appropriate strategy to identify improvements are clearly complex due to the *n*-dimensional space (*i.e.* contributions from energy landscapes, disorder, vacancies, inductive effects, polyanion rotation, *etc.*) that can influence conductivities in these solid electrolytes.

3. Conclusion

An aliovalent series of $Na_{3-2x}Y_{1-x}Nb_xCl_6$ compounds is successfully synthesised using a solvent-free high-energy ball-milling method. Complementary PXRD and NMR reveal a structural threshold upon incorporation of a smaller, more electronegative Nb^{5+} at $Na_2Y_{0.50}Nb_{0.50}Cl_6$, where the unit cell volume shrinks significantly with higher Nb loading. This threshold at $Na_2Y_{0.50}Nb_{0.50}Cl_6$ indicates a single Na chemical environment isostructural with the parent end-member $NaNbCl_6$ and corresponds to the optimal composition with the highest ionic conductivity. Variable-temperature ^{23}Na NMR experiments reveal sodium dynamics on the millisecond (YNb10) and second (YNb0) timescales, demonstrating the importance of Nb substitution for improving sodium-ion conductivity. ^{93}Nb NMR reveals similar chemical environments across Nb loadings; however, a clear shift occurs below YNb50, which correlates with the change in unit cell volume. It appears an intricate combination of interactions play a role in assisting ionic conductivity in these sodium metal halide materials including inductive effect, unit cell expansion enabling the smaller $[NbCl_6]^-$ octahedra to exhibit polyanion rotation and ball-milling inducing structural disorder and the potential of inducing Na vacancies through aliovalent mixing, leading to a reduction in activation energy, thereby enabling more efficient Na^+ conductivity as seen in $Na_2Y_{0.50}Nb_{0.50}Cl_6$.

4. Experimental

4.1 Materials

NaCl (>99.0%, Millipore Sigma), $NbCl_5$ (99.9%, Millipore Sigma), and YCl_3 (99.99%, Millipore Sigma) were stored in an Ar-filled glovebox (O_2 and H_2O < 1 ppm) and used as is.

4.2 Synthesis

Stoichiometric amounts of $(3 - 2x)$NaCl, xNbCl$_5$, and $(1 - x)$ YCl_3 were combined to synthesise mixtures where $x = 0$, 0.10, 0.25, 0.50, 0.75, 0.90, and 1.0. The mixture was loaded into a 50 mL ZrO_2 ball-mill jar with 5 mm ZrO_2 balls occupying approximately one-third of the jar in an Ar-filled glovebox. The ball-mill medium was sealed in the glovebox, transferred to a Retsch PM 100 Planetary Mill, and subjected to 18 cycles at 650 rpm, with rotation reversal at each cycle. Each cycle consists of 45 minutes of milling and 15 minutes of rest.

4.3 Powder X-ray diffraction

Measurements were performed on the Bruker D8 Advance Diffractometer (Cu-Kα_1 (λ = 1.5406 Å) and Kα_2 (λ = 1.5444 Å) radiation) operating in Bragg–Brentano (parafocusing) geometry. Samples were prepared in the glovebox with mineral oil and mounted on a zero-background sample holder rotating at 2 rpm. Diffraction patterns were scanned over a 2θ range of 5–90° with a step size of 0.01° s^{-1}. Phase matching was done in Bruker DIFFRAC.EVA v. 7.2.0.2 against the Crystallography Open Database (COD). Pawley fitting and Rietveld refinements were done in the Topas Academic software package (v. 7.0.0.7).[88] Zero error of the detector and instrumental contribution to peak broadening were refined from Al_2O_3 data, while sample displacement and lattice parameters were freely refined. Where appropriate, the NaCl model was included in the fit and refined using the Rietveld method (while the main phase was still refined in Pawley mode) due to the potential for NaCl peaks to overlap with the main phase. Rietveld allows constraining peak intensities, thus avoiding the possibility of fitting NaCl peaks with the 3-1-6/1-1-6 phase. For that, for NaCl, unit cell parameters, scale, and atomic displacement were fixed at published (unit cell) or manually adjusted values (scale, displacement) through a series of iterations.

4.4 Solid-state nuclear magnetic resonance spectroscopy

The ^{23}Na and ^{93}Nb NMR were performed on a Bruker Avance NEO 500 (B_0 = 11.75 T) and Bruker Advance NEO 800 (B_0 = 18.8 T) spectrometer. A 4-mm triple-resonance (HXY) magic-angle spinning (MAS) probe operating in double-resonance mode was used on the NEO 500 spectrometer. Either a 3.2- or 4-mm double-resonance (HX) MAS probe was used on the NEO 800.

Open Access Article. Published on 26 February 2026. Downloaded on 3/19/2026 5:43:23 PM.
This article is licensed under a Creative Commons Attribution-NonCommercial 3.0 Unported Licence.

All ^{23}Na NMR spectra were referenced to 0.1 M NaCl in D_2O at $\delta(^{23}\text{Na}) = 0.00$ ppm. All ^{93}Nb NMR spectra were indirectly referenced to the ^{23}Na frequency of 0.1 M NaCl in D_2O at $\delta(^{23}\text{Na}) = 0$ ppm.

Variable temperature (VT) ^{23}Na NMR experiments at $B_0 = 11.75$ T were acquired by heating the samples *via* N_2 gas flow through a Bruker BCU II unit (289K $\leq T \leq$ 360 K) under MAS ($\nu_r = 10$ kHz). The samples were corrected for frictional heating and instrumental error using $CH_3NH_3PbCl_3$ as a calibration standard.[89] ^{23}Na NMR spectra were acquired using a Bloch decay pulse sequence with a 4.0 μs π/2 pulse ($\nu_{rf} = 62.5$ kHz), 64 co-added transients, and 15 s recycle delay. Spin–lattice relaxation (T_1) experiments were performed using an inversion recovery pulse sequence with a 4.0 μs π/2 pulse, 16 scans, and 0.1 s recycle delay. The T_1 values were calculated from the peak intensity using a single-exponential decay function: $I_t = I_0 + e^{\frac{-t}{T_1}}$.

Two-dimensional ^{23}Na EXchange SpectroscopY (EXSY) experiments were acquired at $B_0 = 18.8$ T with gas flow through a Bruker BCU II unit (289 K $\leq T \leq$ 325 K) under MAS ($\nu_r = 10$ kHz) using mixing times (τ_{mix}) ranging from 50 μs to 2 s, 10 s recycle delay, 768 slices, and 8 co-added transients per slice. The samples were corrected for frictional heating and instrumental error using the same method described above. Spin–lattice relaxation (T_1) experiments were performed before each EXSY experiment using an inversion recovery pulse sequence with a 2.0 μs π/2 pulse, 8 scans, and 0.1 s recycle delay to ensure mixing times were below the measured T_1.

^{93}Nb NMR measurements were acquired at $B_0 = 11.75$ and 18.8 T. The $B_0 = 11.75$ experiments were acquired using a Hahn echo sequence ($\nu_r = 0$ and 14 kHz) with a 1.87 μs π/2 pulse ($\nu_{rf} = 133.7$ kHz), 512 to 11 200 co-added transients, and 2 to 5 s recycle delays. The $B_0 = 18.8$ T experiments were acquired using a Hahn echo sequence ($\nu_r = 0$ and 14 kHz) with a 2.0 μs π/2 pulse ($\nu_{rf} = 125$ kHz), 70k to 256k co-added transients, and 1 s recycle delay. All NMR spectra were processed with Bruker TopSpin 4.5.0. and fit using ssNake.[90] NMR simulations were performed using WSolids1.[91] Data were plotted and analysed in Origin 2024.

4.5 Powder electrochemical impedance spectroscopy

The synthesised powder sample was loaded into an electrically insulating Al_2O_3 cylindrical die with an inner diameter of 10 mm, then a stainless-steel electrode was subsequently inserted and compressed under 374 MPa for 10 minutes. The die was transferred to a rack with three screws and adjusted with a torque wrench to maintain a compressive pressure of 184 MPa for the following measurements. The amount of the specimen loaded for the measurement was 60 mg for each sample, resulting in ≈360 μm of thickness after compression. The EIS measurement was performed in the temperature range 303 K to 343 K using a potentiostat workstation BioLogic VP200 from 7 MHz to 1 Hz with an amplitude of 10 mV. All preparation for EIS measurements was conducted in a glovebox with humidity and oxygen levels below 0.1 ppm.

4.6 Quantum chemical computations

Density functional theory (DFT) computations were performed using the Cambridge Serial Total Energy Package[92] (CASTEP) with NMR components[93–95] using the gauge-included projector augmented waves (GIPAW) method. NMR parameters are calculated using the Perdew–Burke–Ernzerhof (PBE) generalised gradient approximation (GGA) exchange–correlation functional with on-the-fly generated (OTFG) ultrasoft pseudopotentials *via* zeroth-order regular approximation (ZORA) relativistic effects. CIF files were obtained for NaCl (mp-22862) from Materials Project.[71] CIF files for Na_3YCl_6 (COD ID: 2203822) and $NaNbCl_6$ (COD ID: 8103950) were obtained from the Crystallography Open Database (COD). An initial Monkhorst–Pack (MP) grid was defined by setting the maximum distance between *k*-points to be 0.07 Å^{-1}, corresponding to a 3 × 3 × 1 MP grid for $NaNbCl_6$ and a 2 × 2 × 3 MP grid for Na_3YCl_6. *k*-spacing was stepped iteratively using an extreme basis set accuracy with a 783 eV plane wave cut-off energy until convergence of magnetic shielding parameters was reached within ∼1 ppm. A final MP grid of 6 × 5 × 2 (*k*-spacing of 0.03 Å^{-1}) for $NaNbCl_6$, 5 × 7 × 8 (*k*-spacing of 0.02 Å^{-1}) for Na_3YCl_6 $P2_1/c$, and 16 × 16 × 16 (*k*-spacing of 0.02 Å^{-1}) for NaCl. Magnetic shielding and EFG tensor values were extracted from the final MP grid.

Author contributions

B. B. Phan designed the project, performed the experiments and data analysis, and wrote the manuscript. T. Shuen conducted EIS experiments and data analysis. D. Vrublevskiy provided XRD data analysis and some manuscript review. Q. Yan provided resources and supervised the project. V. K. Michaelis helped design the project, provided experimental feedback, review & editing, and supervised the project.

Conflicts of interest

There are no conflicts to declare.

Data availability

The data supporting this article have been included as part of the supplementary information (SI). Supplementary information: Tables S1 and S2, NMR spectra and further experimental details. See DOI: https://doi.org/10.1039/d5sc10183b.

Acknowledgements

The Natural Sciences and Engineering Research Council (NSERC) of Canada Discovery program, Canada Research Chairs program, and the NTU-UofA Seed program are acknowledged for research support. Q. Y. acknowledges Singapore ASTAR MTC program M23L9b0052. The Chemistry Centre Magnetic Resonance (C^{2}MR) and X-ray diffraction facilities within the College of Natural and Applied Sciences is supported by the Canada Foundation for Innovation (CFI), the Government of Alberta and the Faculty of Science (University of Alberta). B. B. P. is supported by Future Energy Systems through the University of Alberta.

 © 2026 The Author(s). Published by the Royal Society of Chemistry

Open Access Article. Published on 26 February 2026. Downloaded on 3/19/2026 5:43:23 PM.
This article is licensed under a Creative Commons Attribution-NonCommercial 3.0 Unported Licence.

References

1 H. S. Hirsh, Y. Li, D. H. S. Tan, M. Zhang, E. Zhao and Y. S. Meng, *Adv. Energy Mater.*, 2020, **10**, 2001274.
2 J. Huang, K. Wu, G. Xu, M. Wu, S. Dou and C. Wu, *Chem. Soc. Rev.*, 2023, **52**, 4933–4995.
3 D. Searcey, E. Lipton and A. Gilbertson, *N. Y. Times*, 2021.
4 R. B. Kaunda, *J. Energy Nat. Resour. Law*, 2020, **38**, 237–244.
5 K. M. Abraham, *ACS Energy Lett.*, 2020, **5**, 3544–3547.
6 M. Chaudhary, A. Pominov, D. Mumbaraddi, B. Allen, J. Meyer, A. M. Kirchberger, G. M. Bernard, T. Nilges, A. Mar and V. K. Michaelis, *Adv. Funct. Mater.*, 2024, **34**, 2311829.
7 S. Yang, Y. Tang, Y. Yao, S. He, Z. Wu, Y. Yang, H. Pan, X. Rui and Y. Yu, *Mater. Horiz.*, 2025, **12**, 1058–1083.
8 Y. Fujita, R. Yamanaka, D. Suehiro, K. Imai, K. Koga, T. Asakura, K. Motohashi, A. Sakuda and A. Hayashi, *ACS Appl. Energy Mater.*, 2025, **8**, 8216–8223.
9 M. Chaudhary, M. Rawat, E. Springl, D. Weindl, D. Sarkar, A. Yu, D. Vrublevskiy, T. Nilges, A. Mar and V. K. Michaelis, *ACS Mater. Lett.*, 2025, **7**, 3427–3434.
10 J. B. Goodenough, H. Y.-P. Hong and J. A. Kafalas, *Mater. Res. Bull.*, 1976, **11**, 203–220.
11 L. E. Goodwin, P. Till, M. Bhardwaj, N. Nazer, P. Adelhelm, F. Tietz, W. G. Zeier, F. H. Richter and J. Janek, *ACS Appl. Mater. Interfaces*, 2023, **15**, 50457–50468.
12 D. Sarkar, A. Bhattacharya, J. Meyer, A. M. Kirchberger, V. Mishra, T. Nilges and V. K. Michaelis, *J. Am. Chem. Soc.*, 2023, **145**, 19727–19745.
13 M. Akbar, I. Moeez, Y. H. Kim, M. Kim, J. Jeong, E. Lee, A. H. U. Bhatti, J.-H. Park and K. Y. Chung, *Carbon Energy*, 2025, **7**, e717.
14 C. Li, R. Li, K. Liu, R. Si, Z. Zhang and Y.-S. Hu, *Interdiscip. Mater.*, 2022, **1**, 396–416.
15 K. Motohashi, H. Tsukasaki, A. Sakuda, S. Mori and A. Hayashi, *ACS Mater. Lett.*, 2024, **6**, 1178–1183.
16 S. J. Hussain, J. Liu, P.-H. Du, M. A. Nazir, Q. Sun and P. Jena, *ACS Appl. Mater. Interfaces*, 2024, **16**, 14364–14370.
17 Z. Huang, S. Yoshida, H. Akamatsu, K. Hayashi and S. Ohno, *ACS Mater. Lett.*, 2024, **6**, 1732–1738.
18 E. Sebti, J. Qi, P. M. Richardson, P. Ridley, E. A. Wu, S. Banerjee, R. Giovine, A. Cronk, S.-Y. Ham, Y. Shirley Meng, S. Ping Ong and R. J. Clément, *J. Mater. Chem. A*, 2022, **10**, 21565–21578.
19 H. Kwak, J. Lyoo, J. Park, Y. Han, R. Asakura, A. Remhof, C. Battaglia, H. Kim, S.-T. Hong and Y. S. Jung, *Energy Storage Mater.*, 2021, **37**, 47–54.
20 L. Wang, Z. Song, X. Lou, Y. Chen, T. Wang, Z. Wang, H. Chen, W. Yin, M. Avdeev, W. H. Kan, B. Hu and W. Luo, *Small*, 2024, **20**, 2400195.
21 H. Kwak, S. Wang, J. Park, Y. Liu, K. T. Kim, Y. Choi, Y. Mo and Y. S. Jung, *ACS Energy Lett.*, 2022, **7**, 1776–1805.
22 Z. Wei, L. F. Nazar and J. Janek, *Batter. Supercaps*, 2024, **7**, e202400005.
23 S. Yu, K. Kim, B. C. Wood, H.-G. Jung and K. Yoon Chung, *J. Mater. Chem. A*, 2022, **10**, 24301–24309.
24 Y. Yang, S. Yang, X. Xue, X. Zhang, Q. Li, Y. Yao, X. Rui, H. Pan and Y. Yu, *Adv. Mater.*, 2024, **36**, 2308332.
25 K. Tuo, C. Sun and S. Liu, *Electrochem. Energy Rev.*, 2023, **6**, 17.
26 G. Meyer, S. Peter Ax, T. Schleid and M. Irmler, *Z. Anorg. Allg. Chem.*, 1987, **554**, 25–33.
27 R. Li, K. Xu, K. Liu, R. Si and Z. Zhang, *Chem. Mater.*, 2022, **34**, 8356–8365.
28 R. Schlem, A. Banik, M. Eckardt, M. Zobel and W. G. Zeier, *ACS Appl. Energy Mater.*, 2020, **3**, 10164–10173.
29 E. A. Wu, S. Banerjee, H. Tang, P. M. Richardson, J.-M. Doux, J. Qi, Z. Zhu, A. Grenier, Y. Li, E. Zhao, G. Deysher, E. Sebti, H. Nguyen, R. Stephens, G. Verbist, K. W. Chapman, R. J. Clément, A. Banerjee, Y. S. Meng and S. P. Ong, *Nat. Commun.*, 2021, **12**, 1256.
30 Y. Okada, T. Kimura, K. Motohashi, A. Sakuda and A. Hayashi, *Electrochemistry*, 2023, **91**, 077009.
31 B. J. Park, J.-S. Kim, Y. Kim, J. Choe, C. Park, H.-J. Kim, H.-R. Cho, K. H. Shin, J. Lee, J. Choi, J. Kim, H.-W. Lee, Y.-J. Ko, J. Lee, D.-H. Seo and S.-K. Jung, *ACS Energy Lett.*, 2025, **10**, 4242–4251.
32 T. Zhao, A. N. Sobolev, R. Schlem, B. Helm, M. A. Kraft and W. G. Zeier, *ACS Appl. Energy Mater.*, 2023, **6**, 4334–4341.
33 J. Park, J. P. Son, W. Ko, J.-S. Kim, Y. Choi, H. Kim, H. Kwak, D.-H. Seo, J. Kim and Y. S. Jung, *ACS Energy Lett.*, 2022, **7**, 3293–3301.
34 L. Zhou, C. Y. Kwok, A. Shyamsunder, Q. Zhang, X. Wu and L. F. Nazar, *Energy Environ. Sci.*, 2020, **13**, 2056–2063.
35 F. Hussain, P. Yu, J. Zhu, H. Xia, Y. Zhao and W. Xia, *Adv. Theory Simul.*, 2023, **6**, 2200569.
36 J. Liu, S. Wang, Y. Kawazoe and Q. Sun, *ACS Mater. Lett.*, 2023, **5**, 1009–1017.
37 Y. Yang, K. Chen and H. Zhu, *ACS Nano*, 2025, **19**, 35833–35841.
38 K. Kim, D. Park, H.-G. Jung, K. Y. Chung, J. H. Shim, B. C. Wood and S. Yu, *Chem. Mater.*, 2021, **33**, 3669–3677.
39 K. Tuo, F. Yin and C. Sun, *ACS Sustain. Chem. Eng.*, 2024, **12**, 7012–7025.
40 K. Tuo, F. Yin, F. Mi and C. Sun, *J. Energy Chem.*, 2023, **87**, 12–23.
41 K. Tuo, C. Sun, C. A. López, M. T. Fernández-Díaz and J. A. Alonso, *J. Mater. Chem. A*, 2023, **11**, 15651–15662.
42 F. Ling, Z. Wu, J. Feng, Z. Wang, Z. Li, R. Bai, W. Du, H. Huo, X. Rui, H. Pan, Y. Yao and Y. Yu, *Adv. Mater.*, 2026, e21368.
43 C. Fu, Y. Li, W. Xu, X. Feng, W. Gu, J. Liu, W. Deng, W. Wang, A. M. M. Abeykoon, L. Su, L. Zhu, X. Wu and H. Xiang, *Nat. Commun.*, 2024, **15**, 4315.
44 S. Ohno, A. Banik, G. F. Dewald, M. A. Kraft, T. Krauskopf, N. Minafra, P. Till, M. Weiss and W. G. Zeier, *Prog. Energy*, 2020, **2**, 022001.
45 K. Gotoh, *Batter. Supercaps*, 2021, **4**, 1267–1278.
46 B. Zhang, Y. Ji, L. Liang, Q. Zheng, K. Chen and G. Hou, *Chem. Eng. J.*, 2024, **485**, 149879.
47 D. L. Smiley and G. R. Goward, *Chem. Mater.*, 2016, **28**, 7645–7656.
48 P. M. Bayley, N. M. Trease and C. P. Grey, *J. Am. Chem. Soc.*, 2016, **138**, 1955–1961.

Open Access Article. Published on 26 February 2026. Downloaded on 3/19/2026 5:43:23 PM.
This article is licensed under a Creative Commons Attribution-NonCommercial 3.0 Unported Licence.

49 J. Billaud, R. J. Clément, A. R. Armstrong, J. Canales-Vázquez, P. Rozier, C. P. Grey and P. G. Bruce, *J. Am. Chem. Soc.*, 2014, **136**, 17243–17248.
50 M. Gabrijelčič, B. Tratnik, G. Kapun, E. Tchernychova, N. Z. Logar, A. Krajnc, R. Dominko and A. Vizintin, *J. Mater. Chem. A*, 2025, **13**, 1042–1056.
51 S. Zhang, Y. Xu, H. Wu, T. Pang, N. Zhang, C. Zhao, J. Yue, J. Fu, S. Xia, X. Zhu, G. Wang, H. Duan, B. Xiao, T. Mei, J. Liang, X. Sun and X. Li, *Angew. Chem., Int. Ed.*, 2024, **63**, e202401373.
52 E. Ruoff, S. Kmiec and A. Manthiram, *Adv. Energy Mater.*, 2024, **14**(37), 2402091.
53 X. Xu, Q. Gao, L. Tang and W. Chen, *Appl. Phys. Lett.*, 2025, **126**, 171903.
54 G. Wang, S. Zhang, H. Wu, M. Zheng, C. Zhao, J. Liang, L. Zhou, J. Yue, X. Zhu, Y. Xu, N. Zhang, T. Pang, J. Fu, W. Li, Y. Xia, W. Yin, X. Sun and X. Li, *Adv. Mater.*, 2025, **37**, 2410402.
55 B. Karasulu, S. P. Emge, M. F. Groh, C. P. Grey and A. J. Morris, *J. Am. Chem. Soc.*, 2020, **142**, 3132–3148.
56 M. A. Plass, S. Bette, N. Philipp, I. Moundrakovski, K. Küster, R. E. Dinnebier and B. V. Lotsch, *J. Mater. Chem. A*, 2023, **11**, 13027–13038.
57 L.-S. Du, R. W. Schurko, K. H. Lim and C. P. Grey, *J. Phys. Chem. A*, 2001, **105**, 760–768.
58 K. E. Johnston, J. M. Griffin, R. I. Walton, D. M. Dawson, P. Lightfoot and S. E. Ashbrook, *Phys. Chem. Chem. Phys.*, 2011, **13**, 7565–7576.
59 O. B. Lapina, D. F. Khabibulin, A. A. Shubin and V. V. Terskikh, *Prog. Nucl. Magn. Reson. Spectrosc.*, 2008, **53**, 128–191.
60 R. Schlem, S. Muy, N. Prinz, A. Banik, Y. Shao-Horn, M. Zobel and W. G. Zeier, *Adv. Energy Mater.*, 2020, **10**, 1903719.
61 C. Wang, J. Liang, J. T. Kim and X. Sun, *Sci. Adv.*, 2022, **8**, eadc9516.
62 A. Miura, K. Muraoka, K. Maki, S. Kawaguchi, K. Hikima, H. Muto, A. Matsuda, I. Yamane, T. Shimada, H. Ito, Y. Mizuguchi, C. Moriyoshi, H. Nakajima, S. Mori, H. Oike, A. Nakayama, W. Sun, N. C. Rosero-Navarro and K. Tadanaga, *J. Am. Chem. Soc.*, 2024, **146**, 25263–25269.
63 R. D. Shannon, *Acta Crystallogr. A*, 1976, **32**, 751–767.
64 E. Sebti, J. Qi, P. M. Richardson, P. Ridley, E. A. Wu, S. Banerjee, R. Giovine, A. Cronk, S.-Y. Ham, Y. S. Meng, S. P. Ong and R. J. Clément, *J. Mater. Chem. A*, 2022, **10**, 21565–21578.
65 E. Sebti, H. A. Evans, H. Chen, P. M. Richardson, K. M. White, R. Giovine, K. P. Koirala, Y. Xu, E. Gonzalez-Correa, C. Wang, C. M. Brown, A. K. Cheetham, P. Canepa and R. J. Clément, *J. Am. Chem. Soc.*, 2022, **144**, 5795–5811.
66 T. Zhao, B. Samanta, X. M. de Irujo-Labalde, G. Whang, N. Yadav, M. A. Kraft, P. Adelhelm, M. R. Hansen and W. G. Zeier, *ACS Mater. Lett.*, 2024, **6**, 3683–3689.
67 S. Kmiec, E. Ruoff and A. Manthiram, *Angew. Chem., Int. Ed.*, 2025, **64**, e202416979.
68 C. Ma, Z. Yu, J. Fang, Q. Shi, P. Wang, Y. Liu, Z. Liu, R. Monteiro, L. Parreira, H. Chen, Y. Liu, S. Lu, W. Feng, H. Zhu and Y. Zhao, *Angew. Chem., Int. Ed.*, 2026, **65**(2), e18183.
69 J. A. Newnham, A. G. Squires, M. A. Kraft, D. O. Scanlon and W. G. Zeier, *Adv. Energy Mater.*, 2025, **15**, e04067.
70 C. L. Perrin and T. J. Dwyer, *Chem. Rev.*, 1990, **90**, 935–967.
71 A. Jain, S. P. Ong, G. Hautier, W. Chen, W. D. Richards, S. Dacek, S. Cholia, D. Gunter, D. Skinner, G. Ceder and K. A. Persson, *APL Mater.*, 2013, **1**, 011002.
72 J. V. Hanna, K. J. Pike, T. Charpentier, T. F. Kemp, M. E. Smith, B. E. G. Lucier, R. W. Schurko and L. S. Cahill, *Chem.–Eur. J.*, 2010, **16**, 3222–3239.
73 O. B. Lapina, D. F. Khabibulin, K. V. Romanenko, Z. Gan, M. G. Zuev, V. N. Krasil'nikov and V. E. Fedorov, *Solid State Nucl. Magn. Reson.*, 2005, **28**, 204–224.
74 S. Prasad, P. Zhao, J. Huang, J. J. Fitzgerald and J. S. Shore, *Solid State Nucl. Magn. Reson.*, 2001, **19**, 45–62.
75 A. Flambard, L. Montagne, L. Delevoye and S. Steuernagel, *Solid State Nucl. Magn. Reson.*, 2007, **32**, 34–43.
76 I. V. Yakovlev, E. Papulovskiy, E. A. Paukshtis, V. M. Bondareva, A. V. Toktarev, V. I. Zaikovskii and O. B. Lapina, *Appl. Magn. Reson.*, 2019, **50**, 589–597.
77 L.-S. Du, R. W. Schurko, N. Kim and C. P. Grey, *J. Phys. Chem. A*, 2002, **106**, 7876–7886.
78 H. Chen, L. L. Wong and S. Adams, *Acta Crystallogr., Sect. B*, 2019, **75**, 18–33.
79 A. Manthiram and J. B. Goodenough, *J. Power Sources*, 1989, **26**, 403–408.
80 C. Masquelier and L. Croguennec, *Chem. Rev.*, 2013, **113**, 6552–6591.
81 S. P. Culver, A. G. Squires, N. Minafra, C. W. F. Armstrong, T. Krauskopf, F. Böcher, C. Li, B. J. Morgan and W. G. Zeier, *J. Am. Chem. Soc.*, 2020, **142**, 21210–21219.
82 H. Fang and P. Jena, *Nat. Commun.*, 2022, **13**, 2078.
83 Z. Zhang, H. Li, K. Kaup, L. Zhou, P.-N. Roy and L. F. Nazar, *Matter*, 2020, **2**, 1667–1684.
84 M. Jansen, *Angew Chem. Int. Ed. Engl.*, 1991, **30**, 1547–1558.
85 A. Lundén, *Solid State Commun.*, 1988, **65**, 1237–1240.
86 Z. Zhang, P.-N. Roy, H. Li, M. Avdeev and L. F. Nazar, *J. Am. Chem. Soc.*, 2019, **141**, 19360–19372.
87 R. Li, K. Xu, S. Wen, X. Tang, Z. Lin, X. Guo, M. Avdeev, Z. Zhang and Y.-S. Hu, *Nat. Commun.*, 2025, **16**, 6633.
88 A. A. Coelho, *TOPAS-Academic (version 7.0.0.7) Coelho Software*, Brisbane, Austrailia, 2007.
89 G. M. Bernard, A. Goyal, M. Miskolzie, R. McKay, Q. Wu, R. E. Wasylishen and V. K. Michaelis, *J. Magn. Reson.*, 2017, **283**, 14–21.
90 S. G. J. van Meerten, W. M. J. Franssen and A. P. M. Kentgens, *J. Magn. Reson.*, 2019, **301**, 56–66.
91 K. Eichele, *WSolids1 (version 1.21.7)* 2021.
92 S. J. Clark, M. D. Segall, C. J. Pickard, P. J. Hasnip, M. I. J. Probert, K. Refson and M. C. Payne, *Z. Kristallogr. -Cryst. Mater.*, 2005, **220**, 567–570.
93 C. J. Pickard and F. Mauri, *Phys. Rev. B: Condens. Matter Mater. Phys.*, 2001, **63**, 245101.
94 M. Profeta, F. Mauri and C. J. Pickard, *J. Am. Chem. Soc.*, 2003, **125**, 541–548.
95 J. R. Yates, C. J. Pickard and F. Mauri, *Phys. Rev. B: Condens. Matter Mater. Phys.*, 2007, **76**, 024401.

 © 2026 The Author(s). Published by the Royal Society of Chemistry